ADVANCED FUNCTIONAL MATERIALS
www.afm-journal.de

Origin of the Distinct Thermoelectric Transport Properties of Chalcopyrite $ABTe_2$ (A = Cu, Ag; B = Ga, In)

Yu Cao, Xianli Su, Fanchen Meng, Trevor P. Bailey, Jinggeng Zhao, Hongyao Xie, Jian He,* Ctirad Uher, and Xinfeng Tang**

Despite the same crystal structure and homologous constituent elements, the chalcopyrite compounds $ABTe_2$ (A = Cu, Ag; B = Ga, In) exhibit distinct electronic and thermal transport properties. The aim of this work is to understand the origin of such discrepancy employing experiments and theoretical calculations. The results of Hall coefficient measurements, absorption spectroscopy, and electronic transport studies suggest the deep-level in-gap states induced by the native A-site vacancies play a key role in the observed intrinsic semiconductor to degenerate semiconductor transition and are the origins of the distinct electrical conductivity among $ABTe_2$ compounds. In addition, the cryogenic heat capacity measurements and calculated phonon dispersion relations show that the acoustic and low-frequency optical modes of $AgGaTe_2$ and $AgInTe_2$ are governed by the vibrations of Ag—Te clusters while the counterparts of $CuGaTe_2$ and $CuInTe_2$ compounds are dominated by the vibrations of Te atoms, and the coupling between the acoustic and low-frequency optical modes is notably different among $ABTe_2$ compounds. Specifically, lower avoided-crossing frequencies, lower sound velocity together with stronger Umklapp process yield lower thermal conductivities of $AgGaTe_2$ and $AgInTe_2$ than $CuGaTe_2$ and $CuInTe_2$. This work provides new insights into the understanding and improvement of electrical and thermal properties toward higher thermoelectric performance of chalcopyrite compounds.

1. Introduction

In the past couple of decades, the increasing energy and environmental crises have made the development of environment-friendly renewable energy materials and related energy conversion technologies a research focus worldwide.[1–4] Thermoelectric materials that can accomplish efficient conversion between heat and electricity have attracted much attention.[5–9] The conversion efficiency of thermoelectric material is evaluated by its dimensionless figure of merit $ZT = \frac{\sigma S^2 T}{\kappa}$, where σ, S, κ, and T are the electrical conductivity, the Seebeck coefficient, the total thermal conductivity, and the absolute temperature, respectively. Toward an efficient thermoelectric material, both its electrical conductivity and Seebeck coefficient should be as large as possible, while its ability to conduct heat should be minimized.[10–12] Though there is no known theoretical limit for maximum ZT, the strong and adverse coupling among the σ, S, and κ makes the improvement of ZT a challenge in practice. Numerous investigations document[13–17] that among the effective strategies to boost the thermoelectric performance are appropriate levels of doping, formation of solid solutions, and nanostructuring, including nanocomposite materials. Through the above strategies, high thermoelectric performance has been achieved in PbTe-based materials,[18–20] BiSbTe alloys,[21–23] filled skutterudites,[24–26] SnTe-based materials,[27–29] and BiCuSeO[30–32] over a wide temperature range. Nevertheless, there is always an urgent need for developing new thermoelectric materials.

In recent years, compounds with the diamond-type structure, such as $AgGaTe_2$,[33,34] Cu_2SnX_3 (X = Se, S),[35–38] and $CuFeS_2$,[39–41] have drawn lots of interests in the field of thermoelectrics due to their highly tunable crystal structures and electronic band structures,[42,43] leading to highly tunable physical properties. For example, a maximum ZT value of 0.5 was obtained at 800 K in pristine $CuGaTe_2$[44] taking advantage of its excellent electrical properties. In addition, with proper doping and forming solid solutions, a higher ZT value of 1.3 at 865 K was achieved in $Cu(Ga_{0.75}In_{0.25})_{0.99}Zn_{0.01}Te_2$.[45] Hence, $ABTe_2$ (A = Cu, Ag; B = Ga, In) compounds hold great promise as potential high-performance thermoelectric materials.

Y. Cao, Prof. X. Su, Dr. H. Xie, Prof. X. Tang
State Key Laboratory of Advanced Technology for Materials Synthesis and Processing
Wuhan University of Technology
Wuhan 430070, China
E-mail: suxianli@whut.edu.cn; tangxf@whut.edu.cn
F. Meng, Prof. J. He
Department of Physics and Astronomy
Clemson University
Clemson, SC 29634, USA
E-mail: jianhe@g.clemson.edu
Dr. T. P. Bailey, Prof. C. Uher
Department of Physics
University of Michigan
Ann Arbor, MI 48109, USA
Prof. J. Zhao
School of Physics
Harbin Institute of Technology
Harbin 150080, China
The ORCID identification number(s) for the author(s) of this article can be found under https://doi.org/10.1002/adfm.202005861.

DOI: 10.1002/adfm.202005861

Of special interest is that despite the same crystal structure and similar constituent elements, the $ABTe_2$ chalcopyrites exhibit very different electronic and thermal transport properties.[33,46–48] Concerning the electrical conductivity at room temperature, $CuGaTe_2$ and $CuInTe_2$[46,47,49] possess electrical conductivities of about 2.1×10^3 and 4.1×10^3 S m^{-1}, respectively, while much lower electrical conductivities of around 0.35 and 4.8 S m^{-1} are obtained for $AgGaTe_2$ and $AgInTe_2$,[50,51] respectively. For the thermal conductivity at 300 K, $AgGaTe_2$ and $AgInTe_2$[50,51] exhibit thermal conductivities of 1.77 and 0.92 W m^{-1} K^{-1}, respectively, whereas the thermal conductivities are 7.40 and 6.60 W m^{-1} K^{-1} for $CuGaTe_2$ and $CuInTe_2$,[46,47] respectively. In light of the isoelectronic substitution between Ag and Cu along with Ga and In, the origin of such discrepancies in both electrical and thermal transport properties is unknown and worth investigation. This is the primary motivation for this work.

Another interesting feature in the pristine $ABTe_2$ chalcopyrites is the intrinsic semiconductor to degenerate semiconductor transition at high temperatures. As known, traditional high-performance thermoelectric materials, such as Bi_2Te_3-based and PbTe-based compounds, etc., are heavily doped semiconductors.[52–54] Due to the onset of intrinsic excitations, the electrical conductivity and the bipolar thermal conductivity of these materials rise dramatically with increasing temperature, and the Seebeck coefficient decreases, degrading the thermoelectric performance. In contrast, the electronic transport properties of the $ABTe_2$ compounds are less affected by the detrimental bipolar effect due to their much larger bandgaps on the order of 1 eV.[34,55–59] More interestingly, we in this work found that the pristine $ABTe_2$ (A = Cu, Ag; B = Ga, In) chalcopyrites exhibit intrinsic semiconductor to degenerate semiconductor transitions between 700 and 800 K, the origin of which is found to be related to the deep-level in-gap states induced by native A-site vacancies.

We also study the profound effects of constituent elements on the chemical bond length, angle, and strength, which in turn affect the phonon dispersion relation and thermal conductivity. Specifically, the analyses of the low-temperature heat capacity and calculated phonon dispersion relations reveal the distinction between the dominance of Ag—Te cluster vibrations in low-frequency phonon spectra of $AgGaTe_2$ and $AgInTe_2$ as opposed to the dominance of Te vibrations in the counterparts of $CuGaTe_2$ and $CuInTe_2$. The extent of the coupling between low-frequency optical phonon and acoustic phonon is distinct, $CuGaTe_2$ and $CuInTe_2$ possess higher avoided-crossing frequencies and sound velocity than $AgGaTe_2$ and $AgInTe_2$. In addition, the weak chemical bonds in $AgGaTe_2$ and $AgInTe_2$ result in a lower sound velocity that in turn enhances the Umklapp process, yielding lower thermal conductivities in $AgGaTe_2$ and $AgInTe_2$.

2. Results and Discussion

2.1. Phase Composition and Microstructure

Figure 1a shows powder X-ray diffraction (XRD) patterns at room temperature. All four samples are single phase with a diamond-type structure and the space group of *I*42*d*. Rietveld refinements were employed to derive the lattice constants, bond lengths, and bond angles, and the results are shown in **Figure 2** and **Table 1**. For conciseness, we choose and discuss $AgGaTe_2$ as an example. The crystal structure of the $AgGaTe_2$ compound is composed of three types of building blocks ($AgTe_4$, $GaTe_4$, and Ag_2Ga_2Te), of which corner-shared $AgTe_4$ and $GaTe_4$ tetrahedrons are interconnected into the 3D diamond-type crystal structure. Two adjacent Ag atoms and two adjacent Ga atoms form a tetrahedron, at the center of which resides a Te atom. The bond length of the Ag—Te bond is 2.76 Å, longer than that of the Ga—Te bond of 2.62 Å. The other three compounds possess a similar structure with somewhat different bond lengths and angles. The lattice parameter along the *a*-axis increases from 6.02 to 6.45 Å in order from $CuGaTe_2$ to $CuInTe_2$, to $AgGaTe_2$, and finally to $AgInTe_2$. Meanwhile, the lattice parameter along *c*-axis increases from 11.94 to 12.65 Å in the order from $CuGaTe_2$ to $AgGaTe_2$ to $CuInTe_2$ and finally to $AgInTe_2$. The lattice constant difference is ascribed to the

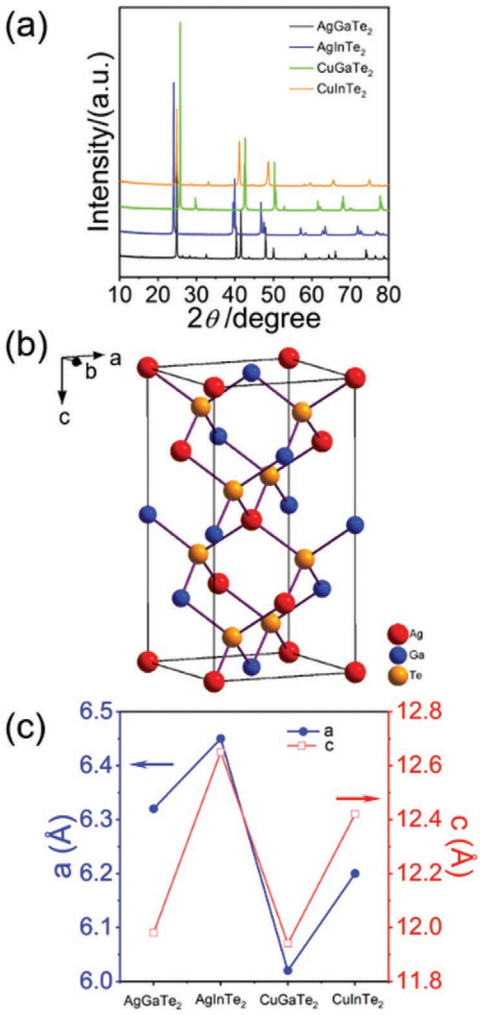

Figure 1. a) Powder XRD patterns of $AgGaTe_2$, $AgInTe_2$, $CuGaTe_2$, and $CuInTe_2$, b) crystal structure of $AgGaTe_2$ at room temperature, where the red spheres represent Ag atoms, the blue spheres represent Ga atoms, and the orange spheres represent Te atoms, and c) the lattice parameters along the *a* and *c* axes of the four compounds.

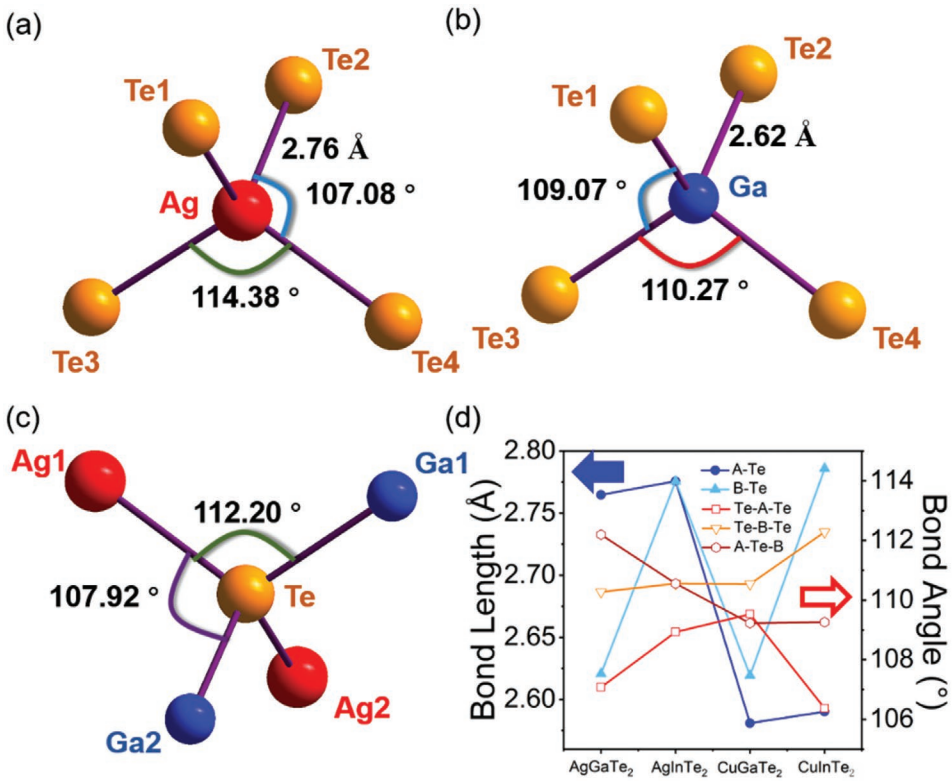

Figure 2. Coordinated environment of a) Ag (center at the tetrahedral structure formed by four Te atoms), b) Ga (center at the tetrahedral structure formed by four Te atoms), c) Te (center at the tetrahedral structure formed by two Ag atoms and two Ga atoms), and d) bond lengths and angles of the four compounds.

distinct chemical bond lengths and angles in the four chalcopyrite compounds, which in turn govern their phonon dispersion relations. Specifically, the Cu—Te bond lengths of 2.58 Å in $CuGaTe_2$ and 2.59 Å in $CuInTe_2$ are shorter than the Ag—Te bond lengths of 2.76 Å in $AgGaTe_2$ and 2.78 Å in $AgInTe_2$. The Cu—Te—Ga bond angle is 109.22° and the Cu—Te—In bond angle is 109.26°, which are closer to the regular tetrahedral angle of 109.5° and smaller than the Ag—Te—Ga bond angle of 112.20° and the Ag—Te—In bond angle of 110.56°.

Concerning the micromorphology, the fracture surfaces are found to have practically the same micromorphology for the four samples. As shown in **Figure 3**, the freshly fractured surface of the $CuGaTe_2$ sample exhibits brittle fracture with transgranular features. The staircase-type cleavage plane is observed with the average grain size of about 20 μm. Close similarities in the microstructure of the four compounds, therefore, rule out the microstructure as the origin of their distinct transport behaviors.

Table 1. Crystal structure parameters including bond angles, bond lengths, and lattice parameters obtained from the structure refinement of the XRD data for $AgGaTe_2$, $AgInTe_2$, $CuGaTe_2$, and $CuInTe_2$.

Parameters		$AgGaTe_2$	$AgInTe_2$	$CuGaTe_2$	$CuInTe_2$
Bond angles [*deg*]	Te—A—Te (I)	107.1	108.9	109.5	106.4
	Te—A—Te (II)	114.4	110.6	109.4	111.0
	Te—B—Te (I)	109.1	108.9	108.9	108.1
	Te—B—Te (II)	110.3	110.6	110.5	112.3
	A—Te—B (I)	107.9	108.9	109.9	109.1
	A—Te—B (II)	112.2	110.6	109.2	109.3
Bond lengths [Å]	A—Te	2.76	2.78	2.58	2.59
	B—Te	2.62	2.78	2.62	2.78
Lattice parameters [Å]	a	6.32	6.45	6.02	6.20
	b	6.32	6.45	6.02	6.20
	c	12.0	12.6	11.9	12.4

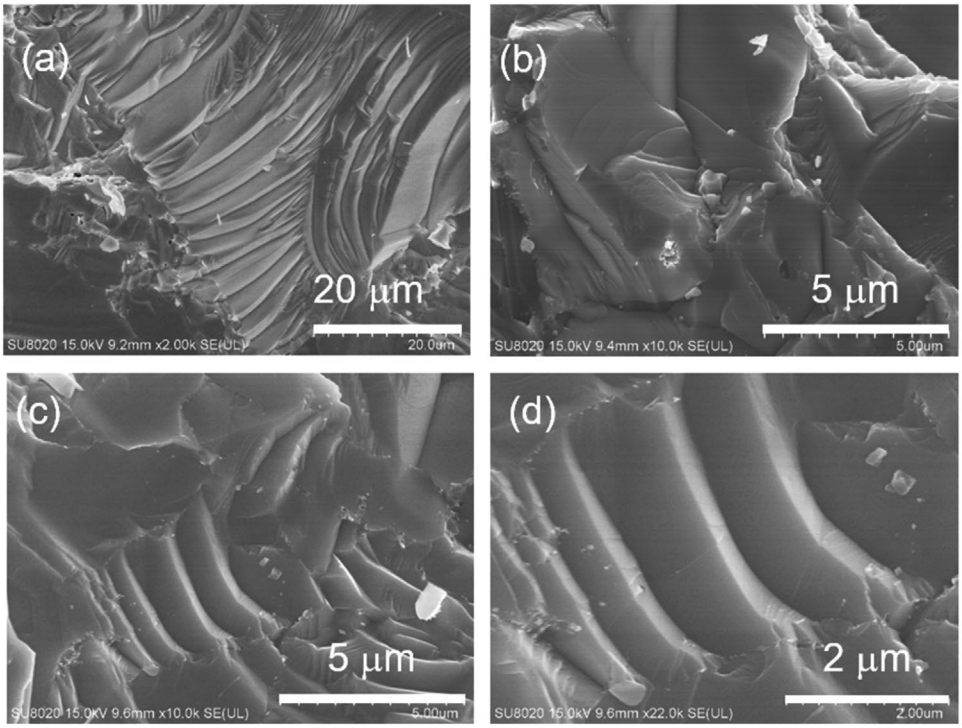

Figure 3. a–d) Field emission scanning electron microscope images of fresh fracture surface in different areas of $CuGaTe_2$ bulk samples with different magnifications.

2.2. Electronic Transport Characterization

2.2.1. Electronic Transport Properties

Figure 4 shows the temperature dependences of the electrical conductivity, Seebeck coefficient, and power factor of the four compounds. As depicted in Figure 4a, unlike the typical electrical conductivity behavior of traditional thermoelectric materials with shallow-level in-gap impurity states, all four compounds undergo an unusual intrinsic semiconductor to degenerate semiconductor transition (crossover). From 300 K to around 750 K, all four compounds behave like semiconductors as their electrical conductivities increase with increasing temperature. However, upon a further increase in temperature, the electrical conductivity levels off and then decreases, the transition is more salient in $AgGaTe_2$ and $AgInTe_2$. The transitions in $AgGaTe_2$ and $AgInTe_2$ take place at temperatures about 100 K lower than in $CuGaTe_2$ and $CuInTe_2$, and the electrical conductivities of the former two compounds are about two orders of magnitude lower than the latter two compounds (e.g., only 1.76×10^2 S m^{-1} for $AgInTe_2$ at 727 K compared to 1.49×10^4 S m^{-1} for $CuGaTe_2$ at the same temperature). Figure 4b shows that all samples exhibit positive Seebeck coefficients over the entire temperature range, indicating that holes are the majority charge carrier. The Seebeck coefficient generally exhibits a temperature dependence opposite to that of electrical conductivities, i.e., the magnitude of the Seebeck coefficient decreases from 300 K, reaches its minimum value between 700 and 800 K, levels off, and then increases at higher temperatures. Due to the excellent electrical conductivity, the $CuGaTe_2$ and $CuInTe_2$ compounds have larger power factors than the $AgGaTe_2$ and $AgInTe_2$ compounds (Figure 4c). The largest power factor of 1.40 mW m^{-1} K^{-2} at 794 K is obtained for the $CuGaTe_2$ compounds, the value is comparable to the traditional thermoelectric materials, such as PbTe[60] and $AgSbTe_2$.[61–63]

2.2.2. Underlying Mechanisms for Electronic Transport

The electronic transport properties of materials are closely related to their electronic band structure and scattering mechanism. The results of temperature variable high-resolution synchrotron powder diffraction measurements[33] indicated that there are no phase transitions from 300 to 850 K. Therefore, the intrinsic semiconductor to degenerate semiconductor transitions observed in the $ABTe_2$ (A = Cu, Ag; B = Ga, In) compounds may be attributed to the change of charge carrier concentration and/or the change of dominant scattering mechanism. Inferring from the temperature-dependent carrier concentration shown in **Figure 5**c, the carrier concentration quickly increases above 600 K. In light of the relatively large value of bandgap (Figure 5b), it suggests the presence of deep-level in-gap impurity states, the thermal excitation of these states populates the valence band with holes and drives the material from a nondegenerate semiconductor to a degenerate semiconductor. The argument is consistent with the temperature variations of electrical conductivity and Seebeck coefficient (cf. Figure 4a,b).

To probe the presence of deep-level in-gap impurity states, the absorption coefficient at different wavelengths was

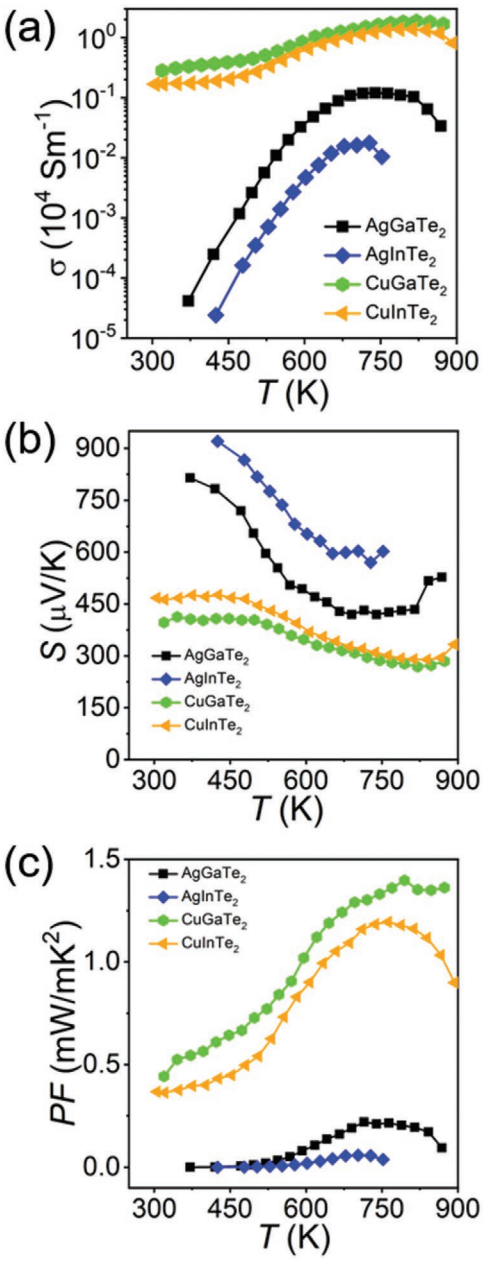

Figure 4. Temperature dependences of a) the electrical conductivity, b) Seebeck coefficient, and c) power factor for $AgGaTe_2$, $AgInTe_2$, $CuGaTe_2$, and $CuInTe_2$.

measured on the four samples (Figure 5a,b). The measured optical bandgaps of $AgGaTe_2$, $AgInTe_2$, $CuGaTe_2$, and $CuInTe_2$ are, respectively, 1.06, 0.87, 1.18, and 0.92 eV, agreeing with the literature data.[34,55,56] Apart from the absorption corresponding to the valence band edge, an additional peak is observed in the optical spectra. The energy value of this extra peak is around 0.43 eV for $AgGaTe_2$ and $AgInTe_2$ samples and 0.63 eV for $CuGaTe_2$ and $CuInTe_2$. Hence, the extra peak, in conjunction with the aforementioned temperature variation of carrier concentration (cf. Figure 5c), indicates the presence of deep-level in-gap impurity states. Assuming the temperature range of 300 to 700 K is within the freeze-out range, the carrier concentration of $CuGaTe_2$ and $CuInTe_2$ as a function of temperature can be expressed as[64]

$$p = \left(\frac{N_A N_V}{2}\right)^{1/2} \exp\left(-\frac{\Delta E_A}{2k_B T}\right) \propto T^{3/4} \exp\left(-\frac{\Delta E_A}{2k_B T}\right) \quad (1)$$

Here, N_A is the concentration of acceptor impurities, N_V is the effective density of states in the valence band proportional to $T^{3/2}$, ΔE_A is the ionization energy given as $\Delta E_A = E_A - E_V$, where E_A is the acceptor level. The ionization energy of impurity level can be obtained from the slope of $\ln(pT^{-3/4})$ versus $1000/T$ curve (cf. the inset of Figure 5c). The derived ionization energies of impurity band in $CuGaTe_2$ and $CuInTe_2$ are 0.52 and 0.61 eV, respectively. These values are fairly close to the values derived from the spectroscopy study discussed above. In addition, the fitting also suggests the presence of shallow impurity levels with the ionization energy of 0.11 and 0.13 eV and a small number of states in $CuGaTe_2$ and $CuInTe_2$.

Based on the data of absorption spectra and Hall coefficient, we draw a schematic electronic band diagram that displays the valence band edge in relation to the conduction band edge, the Fermi level, and the impurity levels in **Figure 6**. There are some common features among these four compounds. First, the Fermi levels of all compounds are located within the bandgap at room temperature. This argument is in accord with that the compounds exhibit semiconducting characteristics in the temperature range from 300 K to around 750 K. The work functions of the four samples are consistent with the values reported in the literature,[65] all falling in the range from 5.3 to 5.6 eV. On the other hand, there are some notable differences among these four compounds. For example, the energies of acceptor impurity levels in $AgGaTe_2$ and $AgInTe_2$ are 0.4 eV above the valence band edge, while they are 0.6 eV above the valence band edge in $CuGaTe_2$ and $CuInTe_2$. The lower ionization energies of impurity levels in $AgGaTe_2$ and $AgInTe_2$ thus explain their lower intrinsic semiconductor to degenerate semiconductor transition temperatures of around 700 K compared with those values of about 800 K in $CuGaTe_2$ and $CuInTe_2$.

The presence of monovalent element vacancies in these compounds is the origin of deep-level states. Shen et al.[44] calculated the formation energies of several kinds of defects in $AgGaTe_2$ and $CuGaTe_2$. They found the formation energies of Cu vacancy in $CuGaTe_2$ and Ag vacancy in $AgGaTe_2$ with the values of 0.27 and 0.62 eV, respectively, are much smaller than the formation energies of other possible defects. Ag or Cu vacancies act as acceptors, consistent with the p-type conduction. In the pseudo-binary phase diagram of A_2Te-B_2Te_3,[66,67] $ABTe_2$ compounds are not line phases, and a trace amount of compositional deviation from the nominal content would result in the Ag and Cu vacancies. Hence, the Ag and Cu vacancies induced deep levels govern the distinct semiconductor behavior in electronic transport characteristics of the four compounds from 300 K to around 750 K.

2.3. Thermal Transport Characterization

2.3.1. Thermal Transport Properties

The temperature dependences of the total thermal conductivity, carrier thermal conductivity, lattice thermal conductivity, and

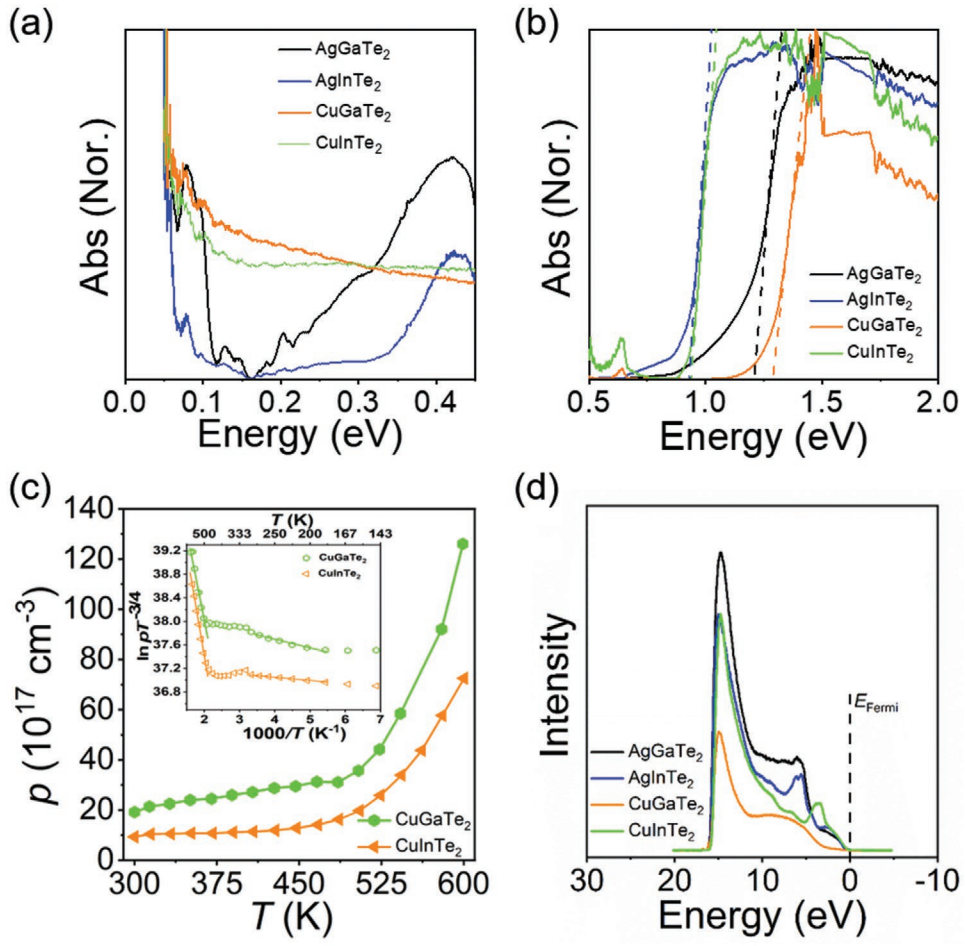

Figure 5. a) Fourier-transformed infrared spectra and b) UV–vis absorption spectra for $AgGaTe_2$, $AgInTe_2$, $CuGaTe_2$, and $CuInTe_2$, c) temperature dependences of carrier concentration for $CuGaTe_2$ and $CuInTe_2$ compounds, and d) ultraviolet photoelectron spectroscopy (UPS) for $AgGaTe_2$, $AgInTe_2$, $CuGaTe_2$, and $CuInTe_2$. The inset in (c) plots $\ln(pT^{-3/4})$ versus $1000/T$ for $CuGaTe_2$ and $CuInTe_2$.

ZT values are presented in **Figure 7**. As discussed in Section 2.2.1, the electrical conductivities of the four compounds exhibit intrinsic semiconductor to degenerate semiconductor transitions. The total thermal conductivities of the four compounds decrease with increasing temperature in the temperature range studied. The carrier thermal conductivity (Figure 7b) can be estimated from the measured electrical conductivity σ by employing the Wiedemann–Franz law,[68,69] $\kappa_e = L\sigma T$. In this formula, L represents the Lorenz number that can be calculated from Equation (2) with the assumption that the electronic band structure of the materials approximately satisfies a single parabolic band model

$$L = \left(\frac{k_B}{e}\right)^2 \left\{\frac{(r+7/2)F_{r+5/2}(\eta)}{(r+3/2)F_{r+1/2}(\eta)} - \left[\frac{(r+5/2)F_{r+3/2}(\eta)}{(r+3/2)F_{r+1/2}(\eta)}\right]^2\right\} \quad (2)$$

Here, η is the reduced Fermi energy calculated from the measured Seebeck coefficient α via combining Equations (3) and (4)

$$\alpha = \pm\frac{k_B}{e}\left[\frac{(r+5/2)F_{r+3/2}(\eta)}{(r+3/2)F_{r+1/2}(\eta)} - \eta\right] \quad (3)$$

$$F_n(\eta) = \int_0^\infty \frac{\chi^n}{1+e^{\chi-\eta}}d\chi \quad (4)$$

In Equations (2) and (3), k_B stands for the Boltzmann constant, e represents the electron charge, and r is the scattering factor, taken here equal to –1/2 for acoustic phonon scattering. The contribution of the charge carriers to the overall thermal conductivity is relatively small because of rather poor electrical conductivities of the compounds. The lattice thermal conductivity thus dominates the total thermal conductivity. As illustrated in the inset of Figure 7c, the lattice thermal conductivity decreases dramatically with increasing temperature, the inverse temperature dependence is the signature of Umklapp process. The lattice thermal conductivities of $CuGaTe_2$ and $CuInTe_2$ compounds are significantly larger than those of $AgGaTe_2$ and $AgInTe_2$, particularly at low temperatures. As shown in Figure 7a, the total thermal conductivity of $CuInTe_2$ is 5.9 W m^{-1} K^{-1} at 300 K, while that of $AgInTe_2$ is 1.4 W m^{-1} K^{-1} at 300 K. The Cu-containing compounds show a much sharper decrease in their thermal conductivity than the Ag-containing compounds, consistent with the larger average sound velocity, higher Grüneisen parameters γ calculated from the sound velocity measured $v$ia the pulse-echo

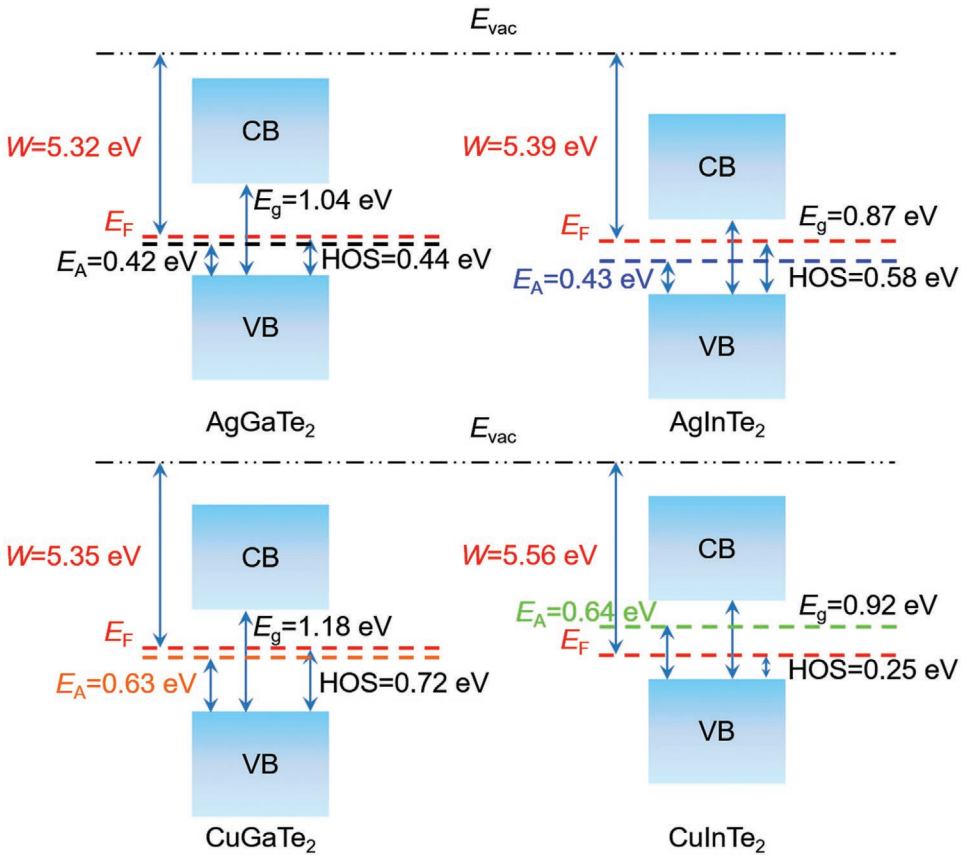

Figure 6. a–d) The electronic band structure diagrams of $AgGaTe_2$, $AgInTe_2$, $CuGaTe_2$, and $CuInTe_2$, where the Evac W, E_F, E_A, E_g, and HOS represent the vacuum level, work function, Fermi level, ionization energy, bandgap, and highest occupied state, respectively.

method (Table 3) and the larger coupling between acoustic phonons and low-frequency optic phonons of the Cu-containing compounds. At 873 K, $CuInTe_2$ and $AgInTe_2$ reach values of 0.98 and 0.23 W m^{-1} K^{-1}, respectively. With both electrical and thermal properties considered, despite rather high thermal conductivities of $CuGaTe_2$ and $CuInTe_2$ compounds, their ZT values reach above 0.9 at 873 K. In contrast, the performance of the $AgGaTe_2$ and $AgInTe_2$ compounds is inferior, the maximum ZT value of $AgGaTe_2$ not exceeding 0.5 and that of $AgInTe_2$ reaching merely 0.2 (cf. Figure 7d).

2.3.2. Underlying Mechanisms for Thermal Transport

To give more insights into the differences in thermal transport properties among the four compounds, we measured the low-temperature heat capacity from 2 to 300 K, the data are displayed in **Figure 8**a. As the temperature increase, more phonon modes are excited, the heat capacity increases steadily and reaches the Dulong–Petit limiting value of 99.8 J mol^{-1} K^{-1} for $ABTe_2$ compounds at 300 K. In the temperature range between 2 and 16 K, the experimental heat capacity can be fitted well using a Debye–Einstein model (Equation (5))

$$\frac{C_p}{T^3}=\frac{\gamma}{T^2}+b+\sum_{i=1}^{n}\frac{A_i(\theta_{Ei})^2}{T^5}\cdot\frac{e^{\theta_{Ei}/T}}{\left(e^{\theta_{Ei}/T}-1\right)^2} \quad (5)$$

The first term in Equation (5) represents the contribution from electrons with the coefficient γ given by Equation (6)

$$\gamma=\frac{\pi^2}{3}k_B^2N(E_F)=1.36\times10^{-4}\times V_{mol}^{\frac{2}{3}}n_\gamma^{\frac{1}{3}}\frac{m^*}{m_0} \quad (6)$$

Here, V_{mol} is the molar volume, n_γ is the number of electrons, m^* is the density of states effective mass, and m_0 is the bare electron mass. The γ term can be ignored because the four compounds are practically insulating at low temperatures. The second term in Equation (5) stands for the Debye phonon modes with b given by Equation (7)

$$b=\frac{12C\pi^4N_Ak_B}{5\theta_D^3} \quad (7)$$

The parameter C follows from the formula $C=1-\sum_i A_i/3NR$, where R is the gas constant and N is the number of atoms per unit cell. The third term in Equation (5) is the contribution from the localized Einstein oscillator modes, and n represents the number of localized Einstein oscillator modes. The amount and the Einstein temperature of the ith Einstein oscillator mode are represented by A_i and E_i, respectively. As shown in Figure 8b, the heat capacity data can be well fitted by two Einstein oscillators in the Debye host.

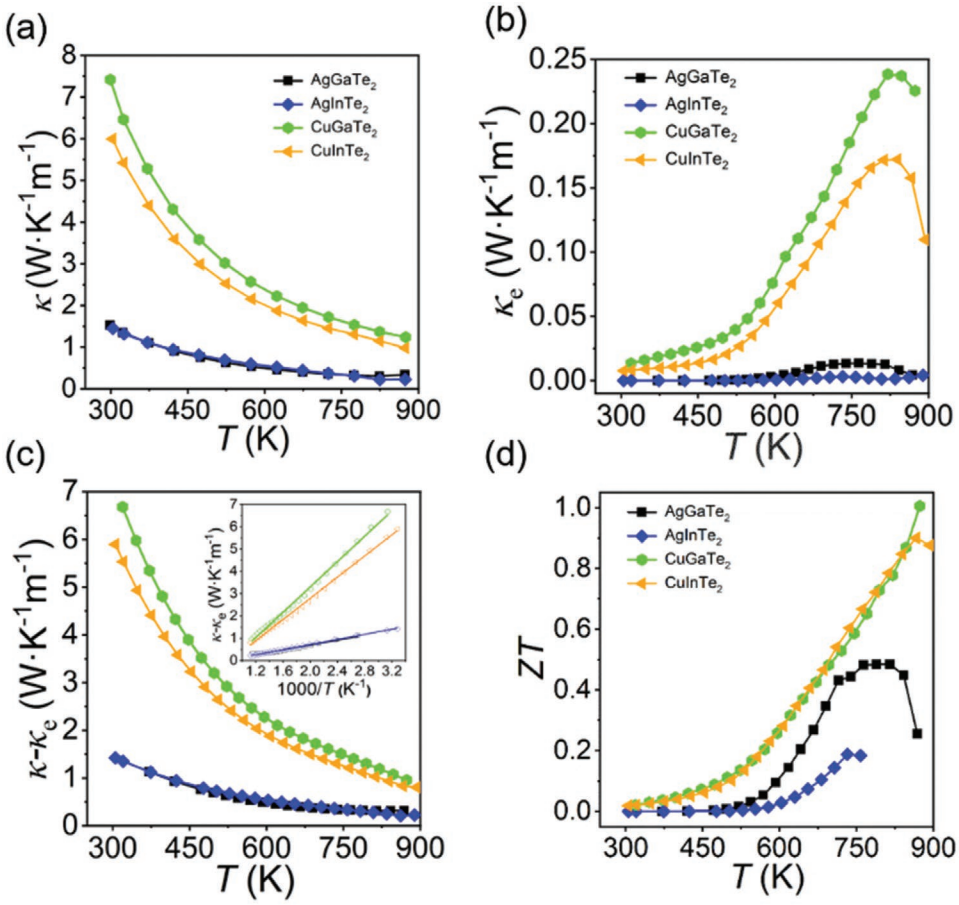

Figure 7. Temperature dependences of a) the total thermal conductivity, b) electronic thermal conductivity, c) lattice thermal conductivity, and d) *ZT* values for $AgGaTe_2$, $AgInTe_2$, $CuGaTe_2$, and $CuInTe_2$. The inset in (c) plots the lattice thermal conductivity versus $1000/T$ to show its inverse dependence on temperature.

The respective fitting parameters, including the Debye temperature and the two Einstein temperatures, are summarized in **Table 2**.

As displayed in Figure 8b, the C_p/T^3 versus T curves for the four compounds substantially deviate from the conventional Debye model $C_p \propto T^3$, exhibiting prominent maxima that we refer to as boson peaks. We observe an interesting correlation: the larger the thermal conductivity, the lower and broader the boson peak.

In practice, the low-temperature heat capacity is typically described by the Debye model in the long-wavelength limit approximation. However, in systems possessing intrinsically low lattice thermal conductivity, such as amorphous structures, glasses, and highly disordered crystal structures, due to the presence of low-frequency oscillator modes, a boson peak is often observed in the plot of C_p/T^3 versus T. The physical origin of the boson peak remains a topic without consensus.[70–80] Some[70] argued that the boson peak arises from the disorder-induced broadening of the transverse acoustic phonons or the Ioffe–Regel crossover at large acoustic wavelengths, also referred to as the van Hove singularity. Others[9,73–75,78] attribute the boson peak to the strong coupling between acoustic phonons and low-frequency optic phonons, which has been observed in $BaAg_2SnSe_4$,[9] Cd_2ReO_7,[78] and $CuFeS_2$.[81] For instance, in $BaAg_2SnSe_4$,[9] the vibrations of the Ag—Se cluster act as two Einstein oscillators in the Debye host. This leads to an ultralow thermal conductivity in $BaAg_2SnSe_4$. Our experimental results obtained on the four $ABTe_2$ compounds suggest the idea that the boson peak arises as a consequence of strong coupling between acoustic phonons and low-frequency optic phonons. Such strong coupling produces a low avoided-crossing frequency for Debye modes in the first Brillouin zone and leads to a low sound velocity. The stronger the coupling, the lower the avoided-crossing frequency and thus the lower thermal conductivity.

To support these arguments, we computed the phonon dispersion relations, phonon density of states, and projected (element-specific) phonon density of states using density functional perturbation theory calculations. As shown in **Figure 9**, strong coupling between acoustic phonons and low-frequency optic phonons is, indeed, observed in the phonon dispersion relations for all four compounds. However, the phonon dispersion relations within the first Brillouin zone differ from each other in several aspects. First, as exhibited in Figure 9, the avoided-crossing frequencies of acoustic phonons for the $AgGaTe_2$ and $AgInTe_2$ compounds are lower than those for $CuGaTe_2$ and $CuInTe_2$ compounds along the

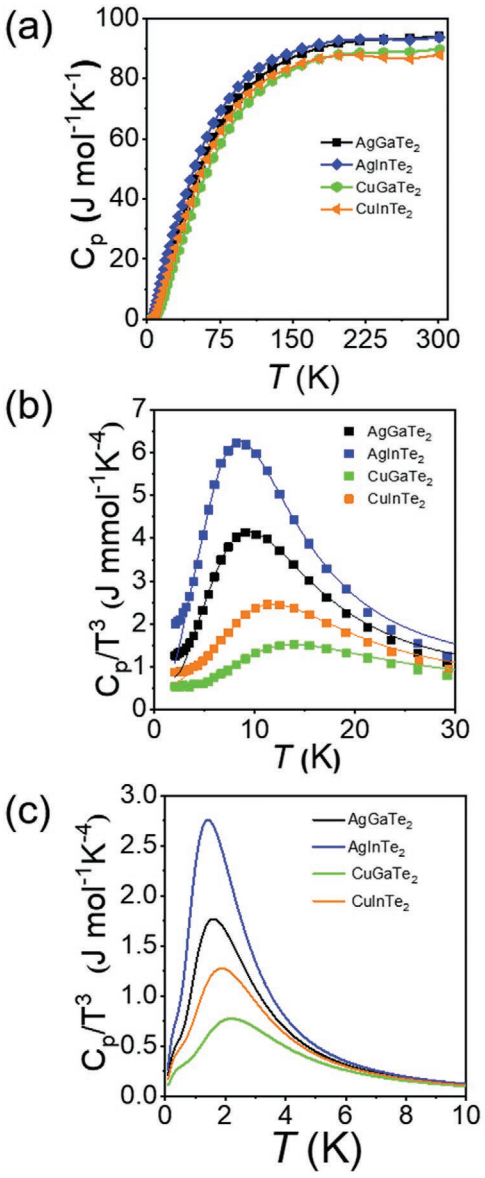

Figure 8. a) Experimental specific heat data from 2 to 300 K, b) the specific heat plotted as C_p/T^3 versus T, the solid lines are the fitting results of a Debye–Einstein model with two Einstein oscillators. The fitting parameters are presented in Table 2. c) The calculated C_p/T^3 for $AgGaTe_2$, $AgInTe_2$, $CuGaTe_2$, and $CuInTe_2$.

Table 2. The fitting parameters of the low-temperature heat capacity data of $AgGaTe_2$, $AgInTe_2$, $CuGaTe_2$, and $CuInTe_2$ by the Debye–Einstein model. Here, b is the Debye lattice term, A_i and Θ_{Ei} are the amplitude and the Einstein temperature of the ith Einstein oscillator mode, and Θ_D is the Debye temperature.

Parameters	$AgGaTe_2$	$AgInTe_2$	$CuGaTe_2$	$CuInTe_2$
b [mJ mol^{-1} K^{-4}]	0.74	0.89	0.57	0.62
A_1	1.46	1.08	1.45	0.51
θ_{E1} [K]	28.4	22.8	49.9	27.8
A_2	17.4	19.8	13.7	17.7
θ_{E2} [K]	52.1	45.7	73.2	61.2
θ_D [K]	124	117	134	132

same direction. In addition, the Ga-containing compounds possess higher avoided-crossing frequencies than the In-containing compounds. For example, the avoided-crossing frequencies for the longitudinal acoustical phonons of $AgGaTe_2$, $AgInTe_2$, $CuGaTe_2$, and $CuInTe_2$ are 38, 35, 53, and 46 cm^{-1}, respectively, which are consistent with the corresponding Einstein temperatures obtained from the low-temperature heat capacity fitting. Such significantly different avoided-crossing frequencies may help explain the distinct thermal conductivities of the four compounds. Specifically, higher avoided-crossing frequencies and sound velocities for the $CuGaTe_2$ and $CuInTe_2$ compounds indicate the smaller phonon densities of states below 40 cm^{-1}, which contributes to their lower and broader boson peak observed in the low-temperature heat capacity. From the smaller slopes in acoustic phonon dispersions of the $AgGaTe_2$ and $AgInTe_2$ compounds compared to those of the $CuGaTe_2$ and $CuInTe_2$ compounds, it follows that the former compounds possess smaller group velocities than the latter compounds. In general, lower group velocities are viewed as a reflection of the lower lattice thermal conductivity and larger anharmonicity in the lattice vibrations.[9,74,82] Specifically, for one transverse acoustic phonons along the Γ–X direction, the slope for $AgInTe_2$ is 1189 m s^{-1}, while the slope for $CuGaTe_2$ is 1765 m s^{-1}. The slopes of the phonon spectra of the four compounds are consistent with the values of the sound velocity measured *via* the pulse-echo method (**Table 3**). The shear sound velocity is 1378 m s^{-1} for $AgGaTe_2$, lower than that for the $CuGaTe_2$ compound of 2081 m s^{-1}. The difference in the average sound velocity partially accounts for the thermal conductivity difference among the four compounds. We conclude that the strong coupling between acoustic phonons and low-frequency optic phonon modes gives rise to a low avoided-crossing frequency of acoustic phonons, which suppresses the sound velocity. The stronger coupling, the lower avoided-crossing frequency of acoustic phonons, and their lower sound velocity result in a lower lattice thermal conductivity.

The calculated projected phonon densities of states for the four compounds reveal contributions of each atom to the phonon spectrum, and specifically to the heat-carrying acoustic modes together with the low-frequency optic phonons. Notably, the vibrations of Ag and Te atoms dominate the acoustic phonon modes in the $AgGaTe_2$ and $AgInTe_2$ compounds, while vibrations of Te atoms are the main contribution in the $CuGaTe_2$ and $CuInTe_2$ compounds. Regarding the low-frequency optic phonon modes (≤30 cm^{-1}), the main contribution comes from the vibrations of the Ag—Te cluster in the $AgGaTe_2$ and $AgInTe_2$ compounds, and the vibrations of Te atoms in the $CuGaTe_2$ and $CuInTe_2$ compounds. Cluster vibrations can substantially scatter the heat-carrying phonons and thus lower the thermal conductivity.[9] All the above considerations lead to the smaller thermal conductivities observed in the $AgGaTe_2$ and $AgInTe_2$ compounds compared to the $CuGaTe_2$ and $CuInTe_2$ structures.

To validate the calculated phonon dispersion relations, the experimental heat capacity was compared with the theoretically calculated heat capacity for each sample obtained with the aid of calculated phonon dispersion relations. According to

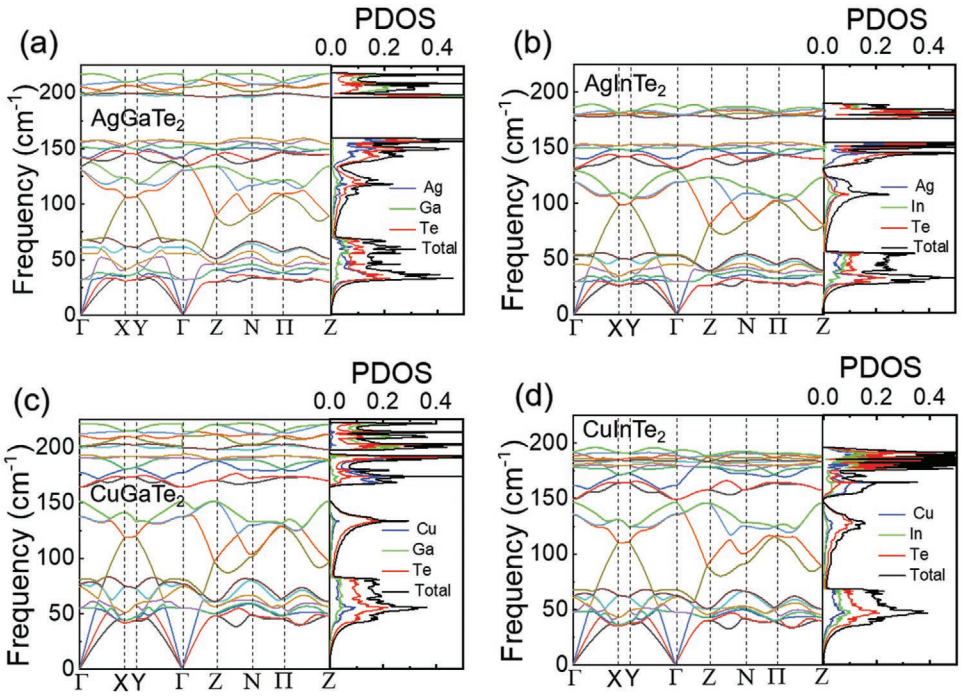

Figure 9. a–d) Calculated phonon dispersions and the corresponding phonon density of states of $AgGaTe_2$, $AgInTe_2$, $CuGaTe_2$, and $CuInTe_2$.

the theory for the specific heat of solids, the heat capacity is obtained from Equation (8)[83]

$$C_V = \left(\frac{\partial \overline{E}}{\partial T}\right)_V = \int_0^{\omega_m} k_B \left(\frac{\hbar\omega}{k_B T}\right)^2 \frac{e^{\hbar\omega/k_B T} g(\omega) d\omega}{\left(e^{\hbar\omega/k_B T} - 1\right)^2} \quad (8)$$

Here, $g(\omega)$ is the phonon density of states, and ω_m represents the maximum frequency in the phonon spectrum that satisfies the following criterion: $\int_0^{\omega_m} g(\omega) d\omega = 3N$, where N is the number of atoms per formula unit. As shown in Figure 8c, the boson peak is observed in the theoretical curve of the temperature-dependent reduced heat capacity (C_p/T^3), and the variation trend is semiquantitatively consistent with the experimental results shown in Figure 8b. The results corroborate that coupling between acoustic phonons and low-frequency optical phonons induces the boson peak in all four compounds. Moreover, the difference in the coupling content among the four compounds contributes to their distinct avoided-crossing frequencies, sound velocities, and thermal conductivities.

Table 3. The measured sound velocities (v_l vs v_a) and the calculated elastic properties (E, G, ν_p, γ, and θ_D) of $AgGaTe_2$, $AgInTe_2$, $CuGaTe_2$, and $CuInTe_2$ at 300 K.

Parameters	$AgGaTe_2$	$AgInTe_2$	$CuGaTe_2$	$CuInTe_2$
Shear sound velocity v_s [m s^{-1}]	1317	1378	2081	1817
Longitudinal sound velocity v_l [m s^{-1}]	2152	2252	3923	3592
Average sound velocity v_a [m s^{-1}]	1454	1521	2326	2037
Young's modulus E [GPa]	24.8	27.2	66.6	52.6
Shear modulus G [GPa]	10.3	11.3	25.5	19.8
Poisson ratio v_p	0.20	0.20	0.30	0.33
Grüeneissen parameter [γ]	1.29	1.29	1.80	1.96
Debye temperature θ_D [K]	139.9	143.3	230.7	195.7

Apart from the intrinsic characteristics of lattice vibrations discussed above, the thermal conductivity is also closely related to the predominant phonon scattering mechanism acting at different temperatures. To evaluate the strength of each phonon scattering mechanism in these four compounds, we have measured the low-temperature thermal conductivities (**Figure 10**a), and have fitted the data using the Debye–Callaway model[84,85]

$$\kappa_L = \frac{k_B}{2\pi^2 v}\left(\frac{k_B}{\hbar}\right)^3 T^3 \int_0^{\frac{\theta_D}{T}} \frac{x^4 e^x}{\tau_c^{-1}\left(e^x - 1\right)^2} dx \quad (9)$$

Here, x is defined as $x = \hbar\omega/k_B T$, and τ_c represents the overall relaxation time. In this study, Umklapp scattering, grain boundary scattering, point defect scattering, and phonon resonance scattering are included. Taking these processes as substantially independent, the relaxation rate is[81,86,87]

$$\begin{aligned}\tau_c^{-1} &= \tau_B^{-1} + \tau_D^{-1} + \tau_U^{-1} + \tau_R^{-1} \\ &= \frac{v}{L} + A\omega^4 + B\omega^2 T e^{-\frac{\theta_D}{3T}} \\ &\quad + \left[\frac{C_1\omega^2}{\left(\omega_1^2 - \omega^2\right)^2} + \frac{C_2\omega^2}{\left(\omega_1^2 - \omega^2\right)^2}\right]\end{aligned} \quad (10)$$

In Equation (10), τ_B, τ_D, τ_U, and τ_R represent the relaxation time for grain boundary scattering, point defect scattering,

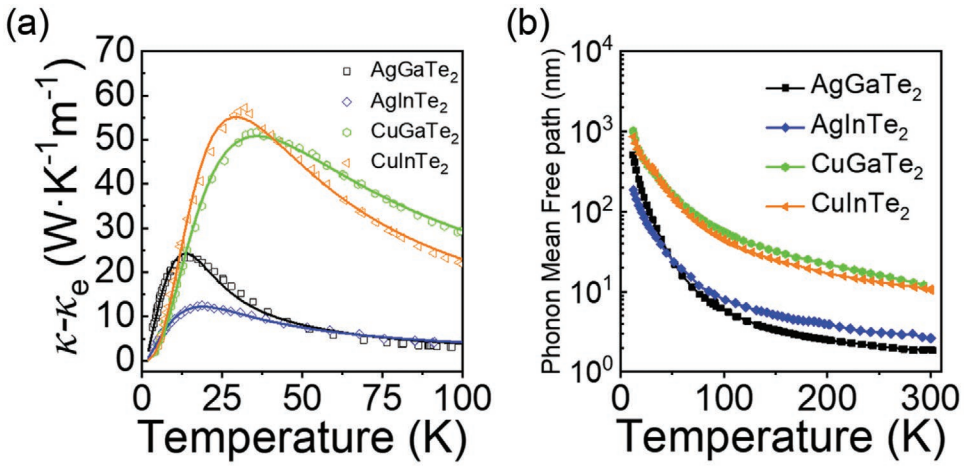

Figure 10. a) Temperature-dependent lattice thermal conductivities of $AgGaTe_2$, $AgInTe_2$, $CuGaTe_2$, and $CuInTe_2$. The solid lines are the calculated curves using the Debye–Callaway model. b) Temperature dependences of the phonon mean free path in the four compounds.

Umklapp scattering, and phonon resonance scattering, respectively. And L is the average grain size in the samples, and constants A and B are the fitting parameters for point defect scattering and Umklapp scattering, respectively. In the fourth term in Equation (10), C_1 and C_2 are constants proportional to the concentration of the oscillators, and ω_1 and ω_2 are the frequencies obtained from fitting the heat capacity. The resulting parameters are presented in **Table 4**. The fraction that each scattering process contributes to the thermal transport, as well as differences among the four samples, can be derived from these parameters. At extremely low temperatures (T < 15 K), grain boundary scattering and point defect scattering dominate the thermal transport process. Hence, the lattice thermal conductivities of the four compounds show little difference with the larger L values in the $AgGaTe_2$ and $AgInTe_2$ samples but the smaller A values in the $CuGaTe_2$ and $CuInTe_2$ samples. As temperature further increases, the Umklapp scattering starts to account for a greater fraction of the lattice thermal conductivity, the larger B parameter values result in lower lattice thermal conductivity of the $AgGaTe_2$ and $AgInTe_2$ compounds. Thus, the different strengths of various scattering processes are also an important factor in understanding the different thermal transport properties of the four compounds. We estimated the phonon mean free path based on a kinetic formulation of the thermal conductivity, $\kappa_L = 1/3\ Cvl$. The dramatically reduced phonon mean free path in the $AgGaTe_2$ and $AgInTe_2$ compounds depicted in Figure 10b further indicates that the propagation of phonons is more strongly impeded in $AgGaTe_2$ and $AgInTe_2$ compounds than in $CuGaTe_2$ and $CuInTe_2$ compounds. Moreover, the Ag-containing compounds show a much sharper decrease below 50 K in their phonon mean free path, indicating stronger coupling between the acoustical phonons and low-frequency optical phonons.

Table 4. The fitting parameters of the low-temperature lattice thermal conductivity of $AgGaTe_2$ by the Debye–Callaway model. Here, L is the grain size, A and B are the constants for point defect scattering, and phonon–phonon scattering, C_1 and C_2, are the constants for phonon resonance scattering.

Compounds	L [μm]	A [10^{-41} s^3]	B [10^{-17} s K^{-1}]	C_1 [10^{33} s^{-3}]	C_2 [10^{33} s^{-3}]
$AgGaTe_2$	19.43	0.67	2.78	1.34	1.34
$AgInTe_2$	5.80	1.09	1.81	1.71	1.71
$CuGaTe_2$	3.23	0.04	0.22	1.71	1.71
$CuInTe_2$	2.85	0.03	0.40	1.71	1.71

3. Conclusions

In this work, the electrical and thermal transport properties of four pristine chalcopyrite compounds $ABTe_2$ (A = Cu, Ag; B = Ga, In) with promising thermoelectric performance are discussed. The underlying mechanism for the distinction of electrical and thermal transport properties among these four compounds with similar crystal chemistry mainly originates from the differences in the character of chemical bonds, the positions of deep-level states, phonon dispersion, anharmonicity, etc. Owing to the ionization process of impurity bands with different ionization energies, different characteristic temperatures of intrinsic semiconductor to degenerate semiconductor transitions and different electrical transport properties are observed. Concerning thermal transport properties, based on the calculated phonon dispersion and compared with $CuGaTe_2$ and $CuInTe_2$ samples, $AgGaTe_2$ and $AgInTe_2$ with the vibrations of Ag—Te clusters possess lower avoided-crossing frequencies and smaller slopes in acoustic phonon dispersions, resulting in lower thermal conductivities and sound velocity in thermal transport properties. Moreover, the calculated phonon dispersion relations reveal that the coupling between acoustic phonons and low-frequency optic phonons plays an important role in the presence of the boson peaks. The discrepancy of thermal conductivity among these four compounds is related to the degree of coupling between the acoustical phonons and low-frequency optical phonons. All the above factors contribute to the highest electrical conductivity of 2.82×10^3 S m^{-1} and thermal conductivity of 7.26 W m^{-1} K^{-1} at 300 K in $CuGaTe_2$, while $AgInTe_2$ sample possesses the lowest electrical conductivity of 1.71×10^{-2} S m^{-1} and thermal conductivity of 1.47 W m^{-1} K^{-1} at 300 K.

4. Experimental Section

Synthesis: High-purity Ag (shot, 99.99%, Sinopharm Chemical Reagent Co., Ltd.), Cu (shot, 99.99%, Sinopharm Chemical Reagent Co., Ltd.), Ga (shot, 99.99%, Sinopharm Chemical Reagent Co., Ltd.), In (shot, 99.99%, Sinopharm Chemical Reagent Co., Ltd.), and Te (shot, 99.999%, Sinopharm Chemical Reagent Co., Ltd.) were weighed and mixed according to the stoichiometric composition of $ABTe_2$ (A = Cu, Ag; B = Ga, In). The mixtures were loaded into evacuated quartz tubes with the inner diameter of 16 mm, and were heated slowly with the heating rate of 100 K h^{-1} to 1273 K, dwelt for 24 h. The quartz tubes were then quenched in supersaturated salt water. Subsequently, the quenched samples were annealed for 24 h at 823 K. The as-obtained ingots were ground into fine powders, which were sintered with the assistance of a spark plasma sintering (SPS) apparatus at 773 K under 45 MPa to obtain fully densified bulk cylindrical samples (ϕ16 × 3.5 mm^3) with a relative density above 98%. The obtained bulks were then cut into proper sizes for structural and transport characterization.

Structure Characterization and Microstructure: The phase composition of the samples was examined by powder XRD analysis (Empyrean, PANalytical; Cu Kα). The working voltage of the electron gun is 40 kV, and the measuring step size is 0.0033 ° with a collecting range from 5 ° to 140 ° to obtain the lattice constants. The morphology of the samples was investigated using field-emission scanning electron microscopy (FESEM, Hitachi SU-8020, Japan).

Thermoelectric Properties Measurement: The electrical conductivity and the Seebeck coefficient from 300 to 873 K were measured under the atmosphere of helium gas by a standard four-probe method (ZEM-3, Ulvac-Riko, Japan). The thermal conductivity was calculated according to the formula $\kappa = DC_p\rho$, where D is the thermal diffusivity measured under the atmosphere of argon gas via a laser flash system (LFA-457, Netzsch, Germany), C_p is the heat capacity calculated by the Dulong–Petit law, and ρ is the density measured by the method of Archimedes. The electrical conductivity, Seebeck coefficient, thermal conductivity, heat capacity, and Hall coefficient at low temperatures were measured by a Physical Property Measurement System (PPMS, Quantum Design, San Diego, CA). The carrier concentration and Hall mobility from 300 to 673 K were measured by a home-made apparatus[88] in the field of 1 Tesla. The carrier concentration (n) and Hall mobility (μ) were calculated according to the following formulas $n = 1/(eR_H)$ and $\mu = \sigma R_H$, where e is the electron charge, R_H is the Hall coefficient, and σ is the electrical conductivity.

Spectral Characterization: The absorption coefficient of the samples from 200 to 2500 nm was measured by a Shimadzu UV-3600 PC double-beam, double-monochromator spectrophotometer. Fourier-transformed infrared spectra from 400 to 4000 cm^{-1} were collected on a Nicolet 6700 IR spectrometer. The working function was measured using UPS (VG Multilab 2000) with samples of standard silver used for calibration.

Calculations of Phonon Dispersion Relations: First-principles calculations based on the density functional theory (DFT) were carried out using Quantum Espresso[89] software. Norm-conserving scalar relativistic pseudopotentials along with the PBE functional under general gradient approximation (GGA)[90] were employed. For geometrical structure relaxation, a Monkhorst–Pack[91] 12 × 12 × 6 k-grid and a cutoff energy of 78 Ry were adopted. The structures were considered as fully relaxed, including the lattice constants and atomic positions, when the energy and force converged to within 10^{-6} Ry and 10^{-5} Ry $Bohr^{-1}$, respectively. With the relaxed structure, density functional perturbation theory (DFPT) was used to calculate the second-order interatomic force constant with a 4 × 4 × 4 q-grid, and therein the phonon dispersion relation and phonon density of states. To obtain the phonon density of states, a find gird of 45 × 45 × 45 was used for sampling the first Brillouin zone.

Acknowledgements

Y.C. and X.S. contributed equally to this work. The authors from the WUT wish to acknowledge support from the National Key Research and Development Program of China (Grant No. 2019YFA0704900), the Natural Science Foundation of China (51972256, 51872219, 51632006, and 51521001), the 111 Project of China (Grant No. B07040), and the Fundamental Research Funds for the Central Universities (WUT: 2020IVB056). The research of T.P.B. and C.U. was supported by a Grant No. DE-SC0018941 from the U.S. Department of Energy.

Conflict of Interest

The authors declare no conflict of interest.

Keywords

boson peaks, chalcopyrites, deep levels, phonon scattering, thermoelectrics

Received: July 12, 2020
Revised: August 27, 2020
Published online: September 18, 2020

[1] G. Tan, L. D. Zhao, M. G. Kanatzidis, *Chem. Rev.* **2016**, *116*, 12123.
[2] K. Biswas, J. He, I. D. Blum, C.-I. Wu, T. P. Hogan, D. N. Seidman, V. P. Dravid, M. G. Kanatzidis, *Nature* **2012**, *489*, 414.
[3] Z. L. Wang, W. Wu, *Angew. Chem., Int. Ed.* **2012**, *51*, 11700.
[4] S. Ortega, M. Ibáñez, Y. Liu, Y. Zhang, M. V. Kovalenko, D. Cadavid, A. Cabot, *Chem. Soc. Rev.* **2017**, *46*, 3510.
[5] X. Su, P. Wei, H. Li, W. Liu, Y. Yan, P. Li, C. Su, C. Xie, W. Zhao, P. Zhai, Q. Zhang, X. Tang, C. Uher, *Adv. Mater.* **2017**, *29*, 1602013.
[6] W. Liu, J. Hu, S. Zhang, M. Deng, C.-G. Han, Y. Liu, *Mater. Today Phys.* **2017**, *1*, 50.
[7] W. Liu, J. Zhou, Q. Jie, Y. Li, H. S. Kim, J. Bao, G. Chen, Z. Ren, *Energy Environ. Sci.* **2016**, *9*, 530.
[8] R. Deng, X. Su, S. Hao, Z. Zheng, M. Zhang, H. Xie, W. Liu, Y. Yan, C. Wolverton, C. Uher, M. G. Kanatzidis, X. Tang, *Energy Environ. Sci.* **2018**, *11*, 1520.
[9] Y. Li, Z. Li, C. Zhang, D. Yang, T. Liu, Y. Yan, W. Liu, G. Tan, X. Su, C. Uher, X. Tang, *Mater. Today Phys.* **2019**, *9*, 100098.
[10] G. J. Snyder, A. H. Snyder, *Energy Environ. Sci.* **2017**, *10*, 2280.
[11] J. He, T. M. Tritt, *Science* **2017**, *357*, eaak9997.
[12] P. Ying, X. Li, Y. Wang, J. Yang, C. Fu, W. Zhang, X. Zhao, T. Zhu, *Adv. Funct. Mater.* **2017**, *27*, 1604145.
[13] X. Su, S. Hao, T. P. Bailey, S. Wang, I. Hadar, G. Tan, T.-B. Song, Q. Zhang, C. Uher, C. Wolverton, X. Tang, M. G. Kanatzidis, *Adv. Energy Mater.* **2018**, *8*, 1800659.
[14] W. G. Zeier, A. Zevalkink, Z. M. Gibbs, G. Hautier, M. G. Kanatzidis, G. J. Snyder, *Angew. Chem., Int. Ed.* **2016**, *55*, 6826.
[15] Q. Zhang, E. K. Chere, J. Sun, F. Cao, K. Dahal, S. Chen, G. Chen, Z. Ren, *Adv. Energy Mater.* **2015**, *5*, 1500360.
[16] S. Anand, K. Xia, T. Zhu, C. Wolverton, G. J. Snyder, *Adv. Energy Mater.* **2018**, *8*, 1801409.
[17] G. Tan, F. Shi, S. Hao, H. Chi, L. D. Zhao, C. Uher, C. Wolverton, V. P. Dravid, M. G. Kanatzidis, *J. Am. Chem. Soc.* **2015**, *137*, 5100.
[18] Y. Xiao, H. Wu, W. Li, M. Yin, Y. Pei, Y. Zhang, L. Fu, Y. Chen, S. J. Pennycook, L. Huang, J. He, L.-D. Zhao, *J. Am. Chem. Soc.* **2017**, *139*, 18732.
[19] K. Ahn, H. Shin, J. Im, S. H. Park, I. Chung, *ACS Appl. Mater. Interfaces* **2017**, *9*, 3766.
[20] W. Li, L. Zheng, B. Ge, S. Lin, X. Zhang, Z. Chen, Y. Chang, Y. Pei, *Adv. Mater.* **2017**, *29*, 1605887.
[21] G. Zheng, X. Su, H. Xie, Y. Shu, T. Liang, X. She, W. Liu, Y. Yan, Q. Zhang, C. Uher, M. G. Kanatzidis, X. Tang, *Energy Environ. Sci.* **2017**, *10*, 2638.
[22] Y. Li, X. Wang, G. Liu, B. Shin, F. Shan, *Scr. Mater.* **2019**, *172*, 88.
[23] G. Zheng, X. Su, X. Li, T. Liang, H. Xie, X. She, Y. Yan, C. Uher, M. G. Kanatzidis, X. Tang, *Adv. Energy Mater.* **2016**, *6*, 1600595.

[24] Y. Tang, R. Hanus, S. Chen, G. J. Snyder, *Nat. Commun.* **2015**, *6*, 7584.
[25] A. Moure, M. Rull-Bravo, B. Abad, A. Del Campo, M. M. Rojo, M. H. Aguirre, A. Jacquot, J. F. Fernandez, M. Martin-Gonzalez, *Nano Energy* **2017**, *31*, 393.
[26] P. Zong, R. Hanus, M. Dylla, Y. Tang, J. Liao, Q. Zhang, G. J. Snyder, L. Chen, *Energy Environ. Sci.* **2017**, *10*, 183.
[27] G. Tan, F. Shi, S. Hao, H. Chi, T. P. Bailey, L. D. Zhao, C. Uher, C. Wolverton, V. P. Dravid, M. G. Kanatzidis, *J. Am. Chem. Soc.* **2015**, *137*, 11507.
[28] G. Tan, S. Hao, R. C. Hanus, X. Zhang, S. Anand, T. P. Bailey, A. J. E. Rettie, X. Su, C. Uher, V. P. Dravid, G. J. Snyder, C. Wolverton, M. G. Kanatzidis, *ACS Energy Lett.* **2018**, *3*, 705.
[29] A. Banik, U. S. Shenoy, S. Saha, U. V. Waghmare, K. Biswas, *J. Am. Chem. Soc.* **2016**, *138*, 13068.
[30] Y.-L. Pei, J. He, J.-F. Li, F. Li, Q. Liu, W. Pan, C. Barreteau, D. Berardan, N. Dragoe, L.-D. Zhao, *NPG Asia Mater.* **2013**, *5*, e47.
[31] L.-D. Zhao, J. He, D. Berardan, Y. Lin, J.-F. Li, C.-W. Nan, N. Dragoe, *Energy Environ. Sci.* **2014**, *7*, 2900.
[32] D. Yang, X. Su, Y. Yan, T. Hu, H. Xie, J. He, C. Uher, M. G. Kanatzidis, X. Tang, *Chem. Mater.* **2016**, *28*, 4628.
[33] X. Su, N. Zhao, S. Hao, C. C. Stoumpos, M. Liu, H. Chen, H. Xie, Q. Zhang, C. Wolverton, X. Tang, M. G. Kanatzidis, *Adv. Funct. Mater.* **2019**, *29*, 1806534.
[34] D. Parker, D. J. Singh, *Phys. Rev. B* **2012**, *85*, 125209.
[35] X. Cheng, Y. You, J. Fu, T. Hu, W. Liu, X. Su, Y. Yan, X. Tang, *J. Alloys Compd.* **2018**, *750*, 965.
[36] Y. Li, G. Liu, T. Cao, L. Liu, J. Li, K. Chen, L. Li, Y. Han, M. Zhou, *Adv. Funct. Mater.* **2016**, *26*, 6025.
[37] L. Xi, Y. B. Zhang, X. Y. Shi, J. Yang, X. Shi, L. D. Chen, W. Zhang, J. Yang, D. J. Singh, *Phys. Rev. B* **2012**, *86*, 155201.
[38] Q. Tan, W. Sun, Z. Li, J.-F. Li, *J. Alloys Compd.* **2016**, *672*, 558.
[39] H. Xie, X. Su, G. Zheng, T. Zhu, K. Yin, Y. Yan, C. Uher, M. G. Kanatzidis, X. Tang, *Adv. Energy Mater.* **2017**, *7*, 1601299.
[40] H. Takaki, K. Kobayashi, M. Shimono, N. Kobayashi, K. Hirose, N. Tsujii, T. Mori, *Mater. Today Phys.* **2017**, *3*, 85.
[41] S. W. Lovesey, K. S. Knight, C. Detlefs, S. W. Huang, V. Scagnoli, U. Staub, *J. Phys.: Condens. Matter* **2012**, *24*, 216001.
[42] L. Xue, B. Xu, D. Zhao, L. Yi, *Intermetallics* **2014**, *55*, 204.
[43] Y. Zhong, P. Wang, H. Mei, Z. Jia, N. Cheng, *Semicond. Sci. Technol.* **2018**, *33*, 065014.
[44] J. Shen, X. Zhang, Z. Chen, S. Lin, J. Li, W. Li, S. Li, Y. Chen, Y. Pei, *J. Mater. Chem. A* **2017**, *5*, 5314.
[45] W. D. Carr, D. T. Morelli, *J. Alloys Compd.* **2015**, *630*, 277.
[46] T. Plirdpring, K. Kurosaki, A. Kosuga, T. Day, S. Firdosy, V. Ravi, G. J. Snyder, A. Harnwunggmoung, T. Sugahara, Y. Ohishi, H. Muta, S. Yamanaka, *Adv. Mater.* **2012**, *24*, 3622.
[47] Z. Xia, G. Wang, X. Zhou, W. Wen, *Mater. Res. Bull.* **2018**, *101*, 184.
[48] R. Liu, Y. Qin, N. Cheng, J. Zhang, X. Shi, Y. Grin, L. Chen, *Inorg. Chem. Front.* **2016**, *3*, 1167.
[49] R. Liu, L. Xi, H. Liu, X. Shi, W. Zhang, L. Chen, *Chem. Commun.* **2012**, *48*, 3818.
[50] Y. Zhong, Y. Luo, X. Li, J. Cui, *Sci. Rep.* **2019**, *9*, 18879.
[51] A. Yusufu, K. Kurosaki, A. Kosuga, T. Sugahara, Y. Ohishi, H. Muta, S. Yamanaka, *Appl. Phys. Lett.* **2011**, *99*, 061902.
[52] R. Funahashi, S. Urata, K. Mizuno, T. Kouuchi, M. Mikami, *Appl. Phys. Lett.* **2004**, *85*, 1036.
[53] J. Androulakis, I. Todorov, D.-Y. Chung, S. Ballikaya, G. Wang, C. Uher, M. Kanatzidis, *Phys. Rev. B* **2010**, *82*, 115209.
[54] Y.-J. Kim, L.-D. Zhao, M. G. Kanatzidis, D. N. Seidman, *ACS Appl. Mater. Interfaces* **2017**, *9*, 21791.
[55] K. C. Mandal, A. Smirnov, U. N. Roy, A. Burger, *Mater. Res. Soc. Symp. Proc.* **2002**, *744*, 131.
[56] J. Shewchun, J. J. Loferski, R. Beaulieu, G. H. Chapman, B. K. Garside, *J. Appl. Phys.* **1979**, *50*, 6978.
[57] J. Krustok, A. Jagomagi, M. Grossberg, J. Raudoja, M. Danilson, *Sol. Energy Mater. Sol. Cells* **2006**, *90*, 1973.
[58] J. Krustok, J. Raudoja, M. Yakushev, R. D. Pilkington, H. Collan, *J. Appl. Phys.* **1999**, *86*, 5305.
[59] A. Jagomägi, J. Krustok, J. Raudoja, M. Grossberg, I. Oja, M. Krunks, M. Danilson, *Thin Solid Films* **2005**, *480*, 246.
[60] Y. Pei, J. Lensch-Falk, E. S. Toberer, D. L. Medlin, G. J. Snyder, *Adv. Funct. Mater.* **2011**, *21*, 241.
[61] H. Wu, S. Chen, T. Ikeda, G. J. Snyder, *Acta Mater.* **2012**, *60*, 6144.
[62] B. K. Min, B. S. Kim, I. H. Kim, J. K. Lee, M. H. Kim, M. W. Oh, S. D. Park, H. W. Lee, *Electron. Mater. Lett.* **2011**, *7*, 255.
[63] B. Du, H. Li, J. Xu, X. Tang, C. Uher, *Chem. Mater.* **2010**, *22*, 5521.
[64] Y. Zhu, Y. Liu, M. Wood, N. Z. Koocher, Y. Liu, L. Liu, T. Hu, J. M. Rondinelli, J. Hong, G. J. Snyder, W. Xu, *Chem. Mater.* **2019**, *31*, 8182.
[65] D. Schmid, M. Ruckh, F. Grunwald, H. W. Schock, *J. Appl. Phys.* **1993**, *73*, 2902.
[66] A. Congiu, L. Garbato, P. Manca, *Mater. Res. Bull.* **1973**, *8*, 293.
[67] P.-W. Chiang, D. F. O'Kane, D. R. Mason, *J. Electrochem. Soc.* **1967**, *114*, 759.
[68] G. Tan, W. G. Zeier, F. Shi, P. Wang, G. J. Snyder, V. P. Dravid, M. G. Kanatzidis, *Chem. Mater.* **2015**, *27*, 7801.
[69] W.-S. Liu, Q. Zhang, Y. Lan, S. Chen, X. Yan, Q. Zhang, H. Wang, D. Wang, G. Chen, Z. Ren, *Adv. Energy Mater.* **2011**, *1*, 577.
[70] A. I. Chumakov, G. Monaco, A. Monaco, W. A. Crichton, A. Bosak, R. Rüffer, A. Meyer, F. Kargl, L. Comez, D. Fioretto, H. Giefers, S. Roitsch, G. Wortmann, M. H. Manghnani, A. Hushur, Q. Williams, J. Balogh, K. Parliński, P. Jochym, P. Piekarz, *Phys. Rev. Lett.* **2011**, *106*, 225501.
[71] V. Lubchenko, P. G. Wolynes, *Proc. Natl. Acad. Sci. USA* **2003**, *100*, 1515.
[72] T. S. Grigera, V. Martín-Mayor, G. Parisi, P. Verrocchio, *Nature* **2003**, *422*, 289.
[73] E. Duval, A. Boukenter, T. Achibat, *J. Phys.: Condens. Matter* **1990**, *2*, 10227.
[74] D. A. Parshin, H. R. Schober, V. L. Gurevich, *Phys. Rev. B* **2007**, *76*, 064206.
[75] H. Tanaka, *J. Phys. Soc. Jpn.* **2001**, *70*, 1178.
[76] A. I. Chumakov, I. Sergueev, U. van Bürck, W. Schirmacher, T. Asthalter, R. Rüffer, O. Leupold, W. Petry, *Phys. Rev. Lett.* **2004**, *92*, 245508.
[77] H. Shintani, H. Tanaka, *Nat. Mater.* **2008**, *7*, 870.
[78] J. He, D. Hitchcock, I. Bredeson, N. Hickman, T. M. Tritt, S. Zhang, *Phys. Rev. B* **2010**, *81*, 134302.
[79] V. Gurevich, D. Parshin, H. Schober, *Phys. Rev. B* **2003**, *67*, 094203.
[80] S. N. Taraskin, Y. L. Loh, G. Natarajan, S. R. Elliott, *Phys. Rev. Lett.* **2001**, *86*, 1255.
[81] H. Xie, X. Su, X. Zhang, S. Hao, T. P. Bailey, C. C. Stoumpos, A. P. Douvalis, X. Hu, C. Wolverton, V. P. Dravid, C. Uher, X. Tang, M. G. Kanatzidis, *J. Am. Chem. Soc.* **2019**, *141*, 10905.
[82] F. Liu, P. Parajuli, R. Rao, P. C. Wei, A. Karunarathne, S. Bhattacharya, R. Podila, J. He, B. Maruyama, G. Priyadarshan, J. R. Gladden, Y. Y. Chen, A. M. Rao, *Phys. Rev. B* **2018**, *98*, 224309.
[83] A. Fischer, E.-W. Scheidt, W. Scherer, D. E. Benson, Y. Wu, D. Eklöf, U. Häussermann, *Phys. Rev. B* **2015**, *91*, 224309.
[84] J. Callaway, *Phys. Rev.* **1959**, *113*, 1046.
[85] J. Callaway, H. C. von Baeyer, *Phys. Rev.* **1960**, *120*, 1149.
[86] J. Cohn, G. Nolas, V. Fessatidis, T. Metcalf, G. Slack, *Phys. Rev. Lett.* **1999**, *82*, 779.
[87] J. Yang, G. P. Meisner, D. T. Morelli, C. Uher, *Phys. Rev. B* **2000**, *63*, 014410.
[88] W. Zhao, Z. Liu, P. Wei, Q. Zhang, W. Zhu, X. Su, X. Tang, J. Yang, Y. Liu, J. Shi, Y. Chao, S. Lin, Y. Pei, *Nat. Nanotechnol.* **2017**, *12*, 55.
[89] P. Giannozzi, S. Baroni, N. Bonini, M. Calandra, R. Car, C. Cavazzoni, D. Ceresoli, G. L. Chiarotti, M. Cococcioni, I. Dabo, A. D. Corso, S. de Gironcoli, S. Fabris, G. Fratesi, R. Gebauer, U. Gerstmann, C. Gougoussis, A. Kokalj, M. Lazzeri, L. Martin-Samos, N. Marzari, F. Mauri, R. Mazzarello, S. Paolini, A. Pasquarello, L. Paulatto, C. Sbraccia, S. Scandolo, G. Sclauzero, A. P. Seitsonen, A. Smogunov, P. Umari, R. M. Wentzcovitch, *J. Phys.: Condens. Matter* **2009**, *21*, 395502.
[90] J. P. Perdew, K. Burke, M. Ernzerhof, *Phys. Rev. Lett.* **1996**, *77*, 3865.
[91] H. J. Monkhorst, J. D. Pack, *Phys. Rev. B* **1976**, *13*, 5188.